

Enforcing essential boundary conditions on domains defined by point clouds

Frank Hartmann ^{*1} and Stefan Kollmannsberger ^{†2}

¹Technische Universität München, Arcisstr. 21, 80333 München, Germany

²Chair of Computational Modeling and Simulation, Technische Universität München, Arcisstr. 21, 80333 München, Germany

Abstract

November 15, 2021

This paper develops and investigates a new method for the application of Dirichlet boundary conditions for computational models defined by point clouds. Point cloud models often stem from laser or structured-light scanners which are used to scan existing mechanical structures for which CAD models either do not exist or from which the artifact under investigation deviates in shape or topology. Instead of reconstructing a CAD model from point clouds via surface reconstruction and a subsequent boundary conforming mesh generation, a direct analysis without pre-processing is possible using embedded domain finite element methods. These methods use non-boundary conforming meshes which calls for a weak enforcement of Dirichlet boundary conditions. For point cloud based models, Dirichlet boundary conditions are usually imposed using a diffuse interface approach. This leads to a significant computational overhead due to the necessary computation of domain integrals. Additionally, undesired side effects on the gradients of the solution arise which can only be controlled to some extent. This paper develops a new sharp interface approach for point cloud based models which avoids both issues. The computation of domain integrals is circumvented by an implicit approximation of corresponding Voronoi diagrams of higher order and the resulting sharp approximation avoids the side-effects of diffuse approaches. Benchmark examples from the graphics as well as the computational mechanics community are used to verify the algorithm. All algorithms are implemented in the FCMLab framework and provided at https://gitlab.lrz.de/cie_sam_public/fcmlab/. Further, we discuss challenges and limitations of point cloud based analysis w.r.t. application of Dirichlet boundary conditions.

Keywords: finite cell method, point clouds, essential boundary conditions

*frank.hartmann@tum.de

†stefan.kollmannsberger@tum.de, Corresponding author

Contents

1	Introduction	3
1.1	Geometric Models	3
1.2	Computation on implicitly defined domains	3
2	Enforcing essential boundary conditions on domains defined by point clouds	5
2.1	Local boundary approximation	5
2.2	Diffuse interface approach	5
2.3	Sharp interface approach	7
2.4	Challenges, limitations and further remarks	10
3	Numerical examples	12
3.1	Annular plate benchmarks	12
3.1.1	Problem definition	12
3.1.2	Numerical Results	13
3.2	Point clouds resembling concave, convex and non-smooth boundaries	16
4	Conclusions	18

1 Introduction

1.1 Geometric Models

Geometric models form the basis of any numerical analysis in computational mechanics. Popular geometric models in this field are based on Constructive Solid Geometry (CSG), Boundary representations (B-rep) or a mixture of both [1]. An in-depth discussion of the advantages and disadvantages w.r.t. computational mechanics is given, for example, in [2]. An interesting extension of B-rep models to volumes are V-rep models [3] which allow for the explicit description of the volume itself. To analyze the mechanical behavior of these structures, it is common engineering practice to generate them in Computer Aided Design systems prior to the production of an artifact.

By contrast, for already existing structures it is often the case that a corresponding CAD model does not exist or that the produced artifact deviates from the CAD geometry. One way of obtaining a simple computer based volumetric model of an existing structure is to scan it using computed tomography (CT-scans) or similar technologies. CT-scans are voxel models and directly describe the volume of an investigated artifact. These can be used as a direct input for a large variety of methods for computational analysis [4, 5, 6, 7, 8].

However, many structures cannot be scanned due to their size or the high attenuation of their material. In such cases, one can resort to optical scanning devices to obtain the shape and topology of existing structures. These scanners deliver oriented point clouds. Oriented point clouds consist of coordinates each of which represents a point on the surface of the scanned structure plus an associated normal vector. The usual step to obtain an analysis suitable model is then to convert the point cloud to a surface mesh. This surface mesh describes a valid closed volume in the sense of a B-rep model¹. The B-rep model is then the starting point of a boundary conforming, volumetric mesh generation. The generated volumetric mesh, which usually consists of (boundary-) conforming tet- or hexahedrals, can then be used as an input to, for example, the finite element method. In many cases it is of course possible to carry out the required pre-processing steps from the acquired shape in form of a point cloud to an analysis suitable mesh. Yet, the generation of such analysis suitable computational models can be expensive and the pipeline is not free from numerous pitfalls. Some of the most common complications are flaws in the surface topology, local over-refinements or other problems due to the tight restrictions on aspect ratios and allowed angles within the mesh, see [2, 9].

Recently, it was demonstrated in [10] that is possible to use point clouds as a direct input for computational mechanical analysis and, thereby, to avoid the multitude of otherwise necessary pre-processing steps. Therein, the key idea is to view the point cloud as a geometrical model which implicitly defines the physical domain of interest. We, therefore, discuss the basic aspects of computational mechanics on implicitly defined domains next.

1.2 Computation on implicitly defined domains

The computation on implicitly defined geometries is ideally suited for embedded domain methods. Numerous such methods exist since the 1960ies [11]. Some more recent variants include CUTfem [12], isogeometric B-Rep analysis [13], immersogeometric analysis [14], the aggregated unfitted finite element method [15], and the finite cell method (FCM) which is used in the paper at hand [16]. We refer to [17] for a detailed review including a collection of relevant literature. Interestingly, the FCM has recently also been picked and further developed by other communities as well (see for example contributions in the area of computer graphics [18]).

All of the embedded domain methods mentioned above have different advantages and disadvantages depending on their field of applications but share a common goal: to avoid boundary conforming

¹i.e. a 2-manifold without a boundary

mesh generation. In the following we present the point of view of the FCM. The FCM extends the physical domain of interest Ω with a fictitious domain, such that their union Ω_e can be meshed easily. Figure 1 depicts this basic idea.

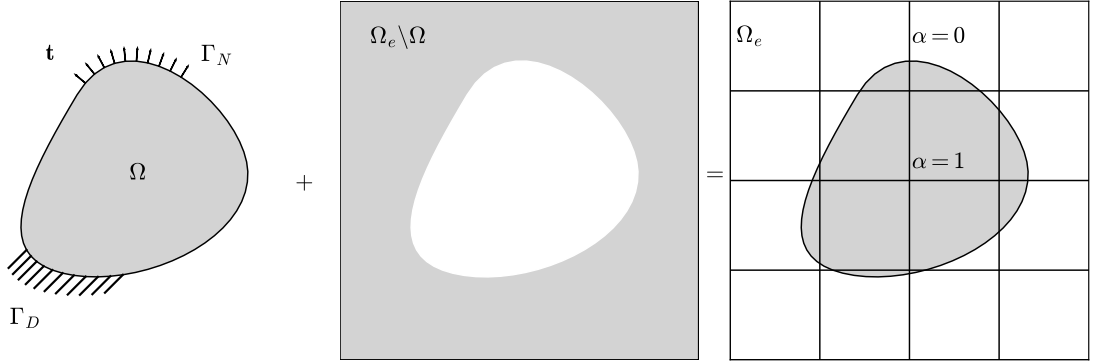


Figure 1: The core concept of the FCM. The physical domain Ω is extended by the fictitious domain $\Omega_e \setminus \Omega$. The extended domain Ω_e can then be meshed easily. To recover the physical domain Ω , the extended domain Ω_e is penalized by $\alpha = 0$ in $\Omega_e \setminus \Omega$.

To solve the linear elastostatic problem the following weak formulation is then used: “Find $\mathbf{u} \in H^1(\Omega_e)$ such that

$$(\alpha \boldsymbol{\sigma}(\mathbf{u}), \nabla \mathbf{w})_{\Omega_e} + \beta \cdot (\mathbf{u}, \mathbf{w})_{\Gamma_D} = (\alpha \mathbf{b}, \mathbf{w})_{\Omega_e} + (\hat{\mathbf{t}}, \mathbf{w})_{\Gamma_N} + \beta \cdot (\hat{\mathbf{u}}, \mathbf{w})_{\Gamma_D} \quad \forall \mathbf{w} \in H^1(\Omega). \quad (1)$$

Here (\cdot, \cdot) , $\boldsymbol{\sigma}$, \mathbf{u} , \mathbf{w} and \mathbf{b} denote the L^2 scalar product, the Cauchy stress tensor, the displacement vector, the test function, and the body forces, respectively. For consistency with the original problem formulated on the physical domain, the following indicator function α is defined:

$$\alpha(\mathbf{x}) = \begin{cases} 1 & \forall \mathbf{x} \in \Omega \\ \alpha_{fic} & \forall \mathbf{x} \in \Omega_e \setminus \Omega \end{cases} \quad (2)$$

where $\alpha_{fic} \ll 1$. Thus, information about the physical domain is accounted for by the function $\alpha(\mathbf{x})$ rather than the mesh itself. To realize Neumann boundary conditions, in our case the traction $\hat{\mathbf{t}}$ on Γ_N , a contour integral needs to be evaluated. The weak formulation presented in eq. (1) contains two additional contour integrals and a scalar parameter β . These stem from the penalty method and enforce the Dirichlet boundary conditions in the weak sense. Thus, the degree to which a solution of eq. (1) will satisfy the prescribed displacement $\hat{\mathbf{u}}$ on Γ_D depends on the choice of β whereby larger values of β yield a stronger enforcement [19]. Other formulations, such as non-symmetric Nitsche versions as presented in [20] or discontinuous Galerkin formulations as presented in [21] would as well be possible.

In principle, the weak formulation given in eq. (1) can be directly applied to various kinds of geometric models as long as a) the indicator function can be defined such that the volumetric terms can be evaluated accurately and b) as long as the contour integrals can be evaluated on those sections of the boundary where either non-zero Neumann or general Dirichlet boundary conditions are imposed.

Point cloud models fall into a similar category as they can be generated from pictures or are directly provided by laser scans of existing artifacts. The direct mechanical analysis of objects described by (oriented) point clouds as presented in [10] used a diffuse approach to evaluate the

contour integrals in eq. (1). However, a diffuse approach carries mainly two disadvantages: a) it causes a large numerical integration effort close to the diffuse boundary, b) it only provides a clear separation between controlling the solution itself or its gradient on the diffuse boundary in its thin limit. However, the thin limit renders the numerical integration unaffordable thus forcing a trade-off between integration effort and accuracy.

The main novelty of the article at hand is the development and numerical investigation of a sharp interface approach which possesses none of these drawbacks.

The structure of the article is as follows: Section 2 introduces the theoretical aspects of the diffuse and the new sharp interface method. Section 3 is dedicated to demonstrate the effectiveness of the sharp interface approach by its application to a benchmark case. Therein, only the more challenging case of the application of Dirichlet boundary conditions is discussed before conclusions are drawn in section 4.

2 Enforcing essential boundary conditions on domains defined by point clouds

This section starts by summarizing the challenge of approximating the boundary locally in section 2.1 to clarify the view onto the subject of imposing boundary conditions in the context of point cloud models and the finite cell method. The necessity to locally approximate the boundary is common to all presented approaches. The diffuse interface approach is then rehearsed in section 2.2 before the new sharp interface approach is presented in section 2.3. This section is then concluded by a discussion of principle challenges and limitations in section 2.4.

2.1 Local boundary approximation

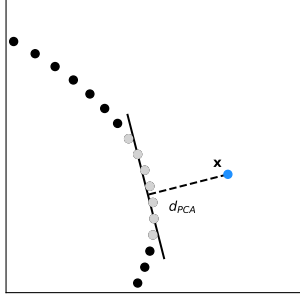
Let $P = \{\mathbf{p}_i\}_{i \in [1, n_{points}]}$ be a point cloud consisting of points which were sampled from a physical boundary Γ with small sampling errors and equal sampling density. Then the point cloud only holds incomplete and noisy information about that boundary. However, each point indicates that the boundary is located somewhere in its close proximity.

To construct an implicit approximation of the boundary we assume that for test points \mathbf{x} , which are in the vicinity of the unknown boundary Γ , a local approximation plane Γ_{PCA, N^k} can be computed from the k -nearest neighbors $N^k(P, \mathbf{x})$ [10]. Figure 2 depicts how a function $d_{\text{PCA}}(P, \mathbf{x})$ giving the unsigned distance to the approximated boundary can be defined based on this assumption.

Querying $N^k(P, \mathbf{x})$ can yield results for which Γ_{PCA, N^k} is invalid. This is for example the case if a test point close to the medial axis of Γ is chosen. Points on the medial axis have multiple sets of closest points on Γ and hence the points in $N^k(P, \mathbf{x})$ are not necessarily neighbors themselves [22]. But this was implied in the construction of Γ_{PCA, N^k} based on $N^k(P, \mathbf{x})$ as depicted in fig. 2a. Therefore the parameter r is introduced to limit the set of points for which Γ_{PCA, N^k} is computed.

2.2 Diffuse interface approach

Assuming $d_{\Gamma_D}(\mathbf{x})$ is a function giving the unsigned distance to the Dirichlet boundary then the zero-set of this function is equivalent to the Dirichlet boundary or $\Gamma_D = \{\mathbf{x} \mid d_{\Gamma_D}(\mathbf{x}) = 0\}$. In Diffuse Boundary Methods the boundary is modeled as a layer $\Gamma_D^\epsilon = \{\mathbf{x} \mid d_{\Gamma_D}(\mathbf{x}) \leq \epsilon\}$ instead, relaxing the sharp interface condition, with $\epsilon \ll 1$ being a parameter controlling the thickness. The approach was proposed in the context of approximating partial differential equations with phase field methods, early works include [23] [24].



(a) Visualization

```

1: procedure  $d_{PCA}(P, \mathbf{x})$ 
2:    $\{\mathbf{p}_i^k\} \leftarrow N^k(P, \mathbf{x})$  ▷ Sorted  $k$ -nearest neighbors
3:   if  $\|\mathbf{p}_1^k - \mathbf{x}\| > r$  then
4:     return  $\|\mathbf{p}_1^k - \mathbf{x}\|$  ▷ Distance to nearest neighbor
5:   else
6:      $\bar{\mathbf{p}} \leftarrow |\{\mathbf{p}_i^k\}|^{-1} \sum_i \mathbf{p}_i^k$  ▷ Tangent plane support point
7:      $C \leftarrow \sum_i (\mathbf{p}_i^k - \bar{\mathbf{p}}) \otimes (\mathbf{p}_i^k - \bar{\mathbf{p}})$  ▷ Covariance matrix
8:      $\bar{\mathbf{n}}_1, \bar{\mathbf{n}}_2 \leftarrow \text{eigenvectors}(C)$  ▷ Tangent plane normal vector
9:     return  $|\bar{\mathbf{n}}_2 \cdot (\mathbf{x} - \bar{\mathbf{p}})|$  ▷ Distance to plane
10:  end if
11: end procedure

```

(b) Procedure to compute $d_{PCA}(\mathbf{x})$

Figure 2: The value assigned to $d_{PCA}(\mathbf{x})$ is either the test point's distance to the least squares fitting plane of its k -nearest neighbors $\{\mathbf{p}_i^k\}$, $i = 1 \dots k$, or the distance to its nearest neighbor \mathbf{p}_1^k . The latter is returned if the test point is not contained within a circle of radius r around \mathbf{p}_1^k .

Leveraging this model and following our intent to compute contour integrals resulting from the penalty method on point cloud data we replace the integral over Γ_D on the left hand side of eq. (1) with

$$\beta \cdot \int_{\Gamma_D} \mathbf{u} \cdot \mathbf{w} \, d\Gamma = \beta \cdot \int_{\Omega_e} \delta(d_{\Gamma_D}) (\mathbf{u} \cdot \mathbf{w}) \, d\Omega \approx \beta \cdot \int_{\Omega_e} \delta^\epsilon(d_{PCA}(P_D, \mathbf{x})) (\mathbf{u} \cdot \mathbf{w}) \, d\Omega. \quad (3)$$

where

$$\delta^\epsilon(x) = \begin{cases} \frac{1}{2\epsilon} (1 + \cos(\frac{\pi x}{\epsilon})) & \text{if } |x| \leq \epsilon \\ 0 & \text{otherwise} \end{cases} \quad (4)$$

Note that this converts the boundary integral into a domain integral by employing the distance function d_{Γ_D} and the Dirac delta distribution $\delta(x)$. In the context of numerical analyses the Dirac delta distribution has to be replaced by a regularized form $\delta^\epsilon(x)$ to make computations feasible, see e.g. [25] for details on this replacement. Lastly, since $d_{\Gamma_D}(\mathbf{x})$ is not known explicitly but given only by a point cloud, $d_{\Gamma_D}(\mathbf{x})$ is replaced with the distance function $d_{PCA}(P_D, \mathbf{x})$. Therein, $P_D \subseteq P$ and P_D are the points belonging to Γ_D . The corresponding boundary integral on the right hand side of eq. (1) is treated accordingly.

Further considerations are necessary for an accurate numerical integration of these terms. Note that the integrand of the resulting domain integral in eq. (3) is only non-zero in a small fraction of Ω_e . Additionally, the polynomial degree of the integrand is increased due to the multiplication with $d_{PCA}(P_D, \mathbf{x})$.

Therefore, a straightforward application of standard quadrature rules to integrate the domain integral containing the diffuse boundary will yield erroneous results. As a remedy, spacetime-based integration schemes may be applied. These subdivide each mesh cell recursively until a specified maximum depth n_{sub}^ϵ is reached. A stopping criterion is defined as follows: subdivide a cell if $\delta(d_{PCA}(P_D, \mathbf{x}_i)) > \epsilon_d$ for any test point \mathbf{x}_i from a suitably dense regular grid². The process is depicted in fig. 3. Subsequently a Gauss-Legendre quadrature of higher order is applied to all subcells of the deepest recursion depth. The same integration scheme is regularly employed in FCM to reduce integration errors resulting from the discontinuity of integrands due to multiplication with $\alpha(\mathbf{x})$.

Now we assume the recursive subdivision rule has been applied to a mesh cell giving n_{sc} subcells. Then the penalty matrix of the cell \mathbf{K}_P^{ce} resulting from discretizing the diffuse term in eq. (3) is

²we chose $\epsilon_d = 10^{-5}$

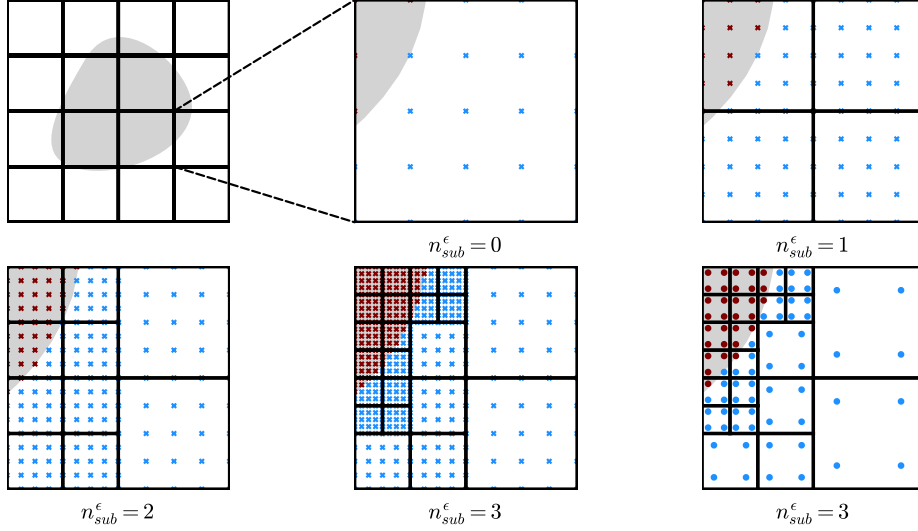


Figure 3: Quadtree for diffuse interface approach: 5 equidistant points \mathbf{x}_i in each direction to test for subdivision until specific subdivision level $n_{sub}^\epsilon = 3$ is reached. Crosses indicate the test points \mathbf{x}_i , dots the integration points (lowest figure to the right).

approximated as follows

$$\mathbf{K}_P^{ce} \approx \beta \cdot \sum_s^{n_{sc}} \sum_j^{n_{gauss}^\epsilon} \sum_i^{n_{gauss}^\epsilon} \delta^\epsilon(d_{PCA}(P_D, \mathbf{x}(\xi_i, \eta_j))) (\mathbf{N}^T \mathbf{N}) \|\mathbf{J}^s\| \|\mathbf{J}^{ce}\|_{\xi_i, \eta_j} v_i v_j. \quad (5)$$

Here n_{gauss}^ϵ , \mathbf{N} , $\|\mathbf{J}^s\|$ and $\|\mathbf{J}^{ce}\|$ denote the number of Gauss-Legendre points in one dimension, the matrix of shape functions, the Jacobian determinant of the subcell, and the Jacobian determinant of the cell, respectively. The Gauss-Legendre coordinates and weights in each dimension are labeled as ξ_i, η_j and v_i, v_j . The penalty vector \mathbf{f}_P^{ce} on the right hand side of eq. (1) is treated analogously.

The degree to which \mathbf{K}_P^{ce} and \mathbf{f}_P^{ce} enforce the prescribed displacement in the respective cell depends on a variety of factors. Comparatively large values need to be chosen for β because the penalty method, unlike Nitsche's method, is an inconsistent method.

However, a large value of β combined with a non-zero ϵ introduces an unwanted coupling between Dirichlet and Neumann boundary conditions. This additional error must be balanced out by a sufficiently low value of β which, in turn, leads to an insufficient approximation of the Dirichlet boundary condition. This dilemma will be clearly pointed out in section 3.1. Therefore, the parameter ϵ should be chosen as small as possible since $\delta^\epsilon(x)$ converges to $\delta(x)$ only for $\epsilon \rightarrow 0$. Unfortunately, the lower bound of ϵ is determined by the effort one wants to spend in the numerical integration. Choosing a smaller ϵ necessitates to increase the subdivision depth of the spacetree to reach the same accuracy. Increasing n_{sub}^ϵ results in exponentially more integration points potentially rendering the numerical integration impractical.

2.3 Sharp interface approach

In this section, we propose a different approach which eliminates the problems mentioned above by omitting the diffuse boundary assumption. Instead, we propose to replace the integral over Γ_D on the left hand side of eq. (1) directly with

$$\beta \cdot \int_{\Gamma_D} \mathbf{u} \cdot \mathbf{w} \, d\Gamma \approx \beta \cdot \int_{\Omega_e} \delta(d_{PCA}(P_D, \mathbf{x})) (\mathbf{u} \cdot \mathbf{w}) \, d\Omega = \beta \cdot \int_{\Gamma_{D,PCA}} \mathbf{u} \cdot \mathbf{w} \, d\Gamma \approx \beta \cdot \int_{\Gamma_{D,sharp}} \mathbf{u} \cdot \mathbf{w} \, d\Gamma \quad (6)$$

and treat the corresponding integral on the right hand side of eq. (1) accordingly. Here we propose that it is possible to integrate over $\Gamma_{D,sharp}$ a domain which is closely related to the zero-set of $d_{PCA}(P_D, \mathbf{x})$ which we will denote by $\Gamma_{D,PCA}$. While this restriction clearly is possible in theory, the crucial question is how an accurate integration of the right hand side eq. (1) can be achieved in a numerical integration scheme as well. But this direct evaluation seems to be a bold move only at first sight.

It follows from intuition that a point \mathbf{p}_i will always be the nearest neighbor if the test point \mathbf{x} is located in its direct vicinity. In fact every point cloud defines a so-called Voronoi diagram which divides the respective space into regions where the nearest neighbor point is the same according to the Euclidean distance [26]. These regions are commonly denoted as Voronoi regions. A generalization are order- k Voronoi diagrams which partition the space into order- k Voronoi regions inside which the k -nearest neighbors of each test point \mathbf{x} are the same. For any of the subsets of cardinality k that can possibly be chosen from a given set of points P in \mathbf{R}^2 the respective order- k Voronoi region is either a convex, possibly unbounded polygon or empty [27]. This includes the classical Voronoi diagram for $k = 1$. Figure 4 depicts the order- k Voronoi diagrams of an exemplary point cloud for different k .

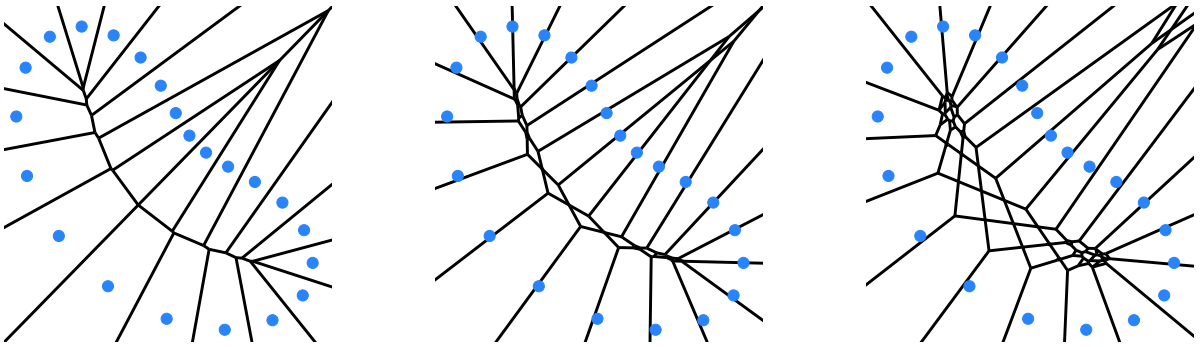


Figure 4: Order- k Voronoi diagrams of an exemplary point cloud for $k = 1, 2, 4$.

From now on we will refer to Voronoi diagrams and Voronoi regions and imply that they are generalized of order k for simplicity. The Voronoi diagram provides an understanding of the reconstructed boundary as given by $d_{PCA}(P_D, \mathbf{x})$. The fact that the k -nearest neighbors are the same within each Voronoi region of the Voronoi diagram implies that the same local approximation plane Γ_{PCA,N^k} is valid in that Voronoi region. Thus, if the Voronoi diagram of P_D is explicitly known, $\Gamma_{D,PCA}$ could be reconstructed in \mathbf{R}^2 as a set of line segments by calculating the points where each Γ_{PCA,N^k} intersects with its respective Voronoi region. Any subsequent numerical integration could, therefore, be carried out directly on these line segments. Unfortunately this intersection problem is much more complex in three dimensions for reasons given in section 2.4. Therefore such an explicit approach would not translate well to three dimensions.

To this end, we will now introduce a scheme that allows numerical integration over $\Gamma_{D,sharp}$ in two dimensions *without having to explicitly compute Voronoi diagrams*. As such it could be logically extended to three dimensions. Although $\Gamma_{D,sharp}$ builds on $\Gamma_{D,PCA}$ they are in general not the same. The scheme works on a per mesh cell basis as common in FCM and consists of two major parts. In the first part depicted in fig. 5 the Voronoi regions that contribute to $\Gamma_{D,PCA}$ in a respective mesh cell are identified. In the second part depicted in fig. 6 the local approximation plane Γ_{PCA,N^k} for each contributing Voronoi region is numerically integrated using a bisection-based scheme.

To identify the Voronoi regions that contribute to $\Gamma_{D,PCA}$ in a respective mesh cell the distance function $d_{PCA}(P_D, \mathbf{x})$ is queried in a structured manner. To this end, the mesh cell in question is partitioned into subcells using a quadtree. A subcell is further subdivided if $d_{PCA}(P_D, \mathbf{x}_c) \leq d_{max}$ holds for the center point of the cell \mathbf{x}_c . Else the subcell is dismissed since it cannot possibly contain parts of $\Gamma_{D,PCA}$. The subdivision process is continued until a maximum subdivision level n_{query}^s is reached. The process to construct this quadtree is depicted in fig. 5 (a)-(d). The rule to construct d_{max} in a subcell is given in fig. 5 (f).

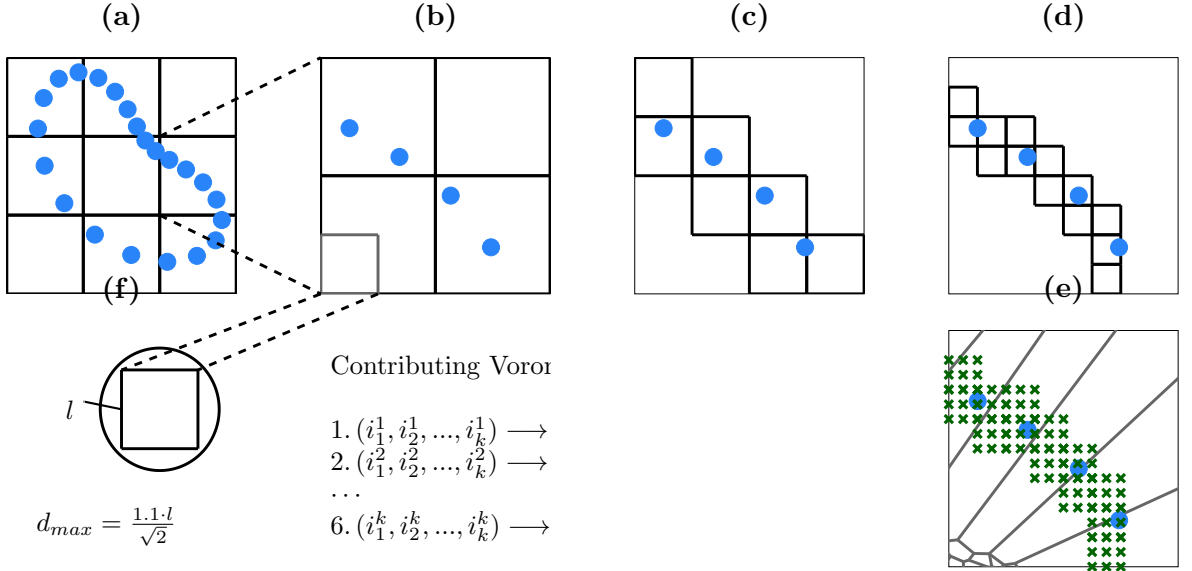


Figure 5: Step 1: finding contributing Voronoi regions. Each of these regions defines one approximation plane Γ_{PCA,N^k} approximating one section of the Dirichlet boundary $\Gamma_{D,PCA}$.

Thus a number of fine grained subcells results for the mesh cell in question. A grid of test points is distributed on each of these subcells and the k -nearest neighbors of each test point are queried as depicted in fig. 5 (e). The core idea is that we can understand each query result as answer to the question in which Voronoi region the test point is located in if the Voronoi regions are identified by the ordered indices of their k nearest neighbors. This is possible since as we remember each subset of k points gives one Voronoi region that is either a convex, possibly unbounded polygon or empty. Hence we can construct a mesh cell specific list of contributing Voronoi regions by collecting the query results as ordered k -tuples of indices and filtering them for uniqueness. In general the maximum subdivision level and test grid have to be chosen such that the test points are dense enough to identify the smallest Voronoi regions that globally contribute to $\Gamma_{D,PCA}$.

Since each Voronoi region corresponds to one local approximation plane Γ_{PCA,N^k} each ordered tuple of indices gives a tuple of support point and normal vector computed as in the distance function $d_{PCA}(P_D, \mathbf{x})$ which is indicated in the center of fig. 5. Therefore, the second part of the scheme iterates through the list of intersection planes found in the first part and applies a bisection-based integration scheme to each plane $(\bar{\mathbf{p}}^j, \bar{\mathbf{n}}_2^j)$. This bisection-based scheme builds on two central assumptions. Firstly we assume that $\bar{\mathbf{p}}^j$ is always inside its respective Voronoi region. Secondly we assume that a global parameter l_{max}^s can be defined to bound the approximation planes. In 2D this results in each plane $(\bar{\mathbf{p}}^j, \bar{\mathbf{n}}_2^j)$ being initialized as a line segment of length l_{max}^s as shown in fig. 6 (a).

The bisection scheme consists in hierarchically subdividing each initiated line segment by querying the k -nearest neighbors for a grid of test points. The subdivisions continue until a predefined level n_{sub}^s . Throughout the process only subsegments that are either fully within the respective

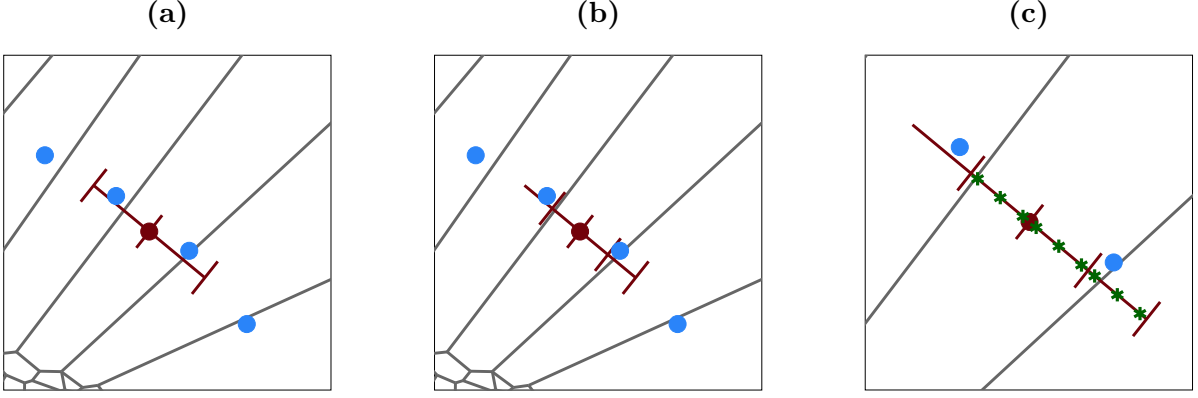


Figure 6: Step 2: Determining the length of the approximated boundary sections Γ_{PCA, N^k} . Their length is defined by their intersection with the boundaries of the Voronoi regions. Since these boundaries are only implicitly known via querying the distance function $d_{\text{PCA}}(P_D, \mathbf{x})$ point wise, the intersection (and therefore the length of the boundary sections) is approximated using a bisection algorithm.

Voronoi region or are intersected by the Voronoi regions are kept. Subsegments that are fully outside the respective Voronoi regions are neglected since they cannot contain any valid integration points (see fig. 6).

Once these two parts have successfully been executed for a mesh cell giving n_{vo} Voronoi regions each providing a line segment with some $n^{\text{vo}, \text{sd}}$ subsegments the penalty matrix of that mesh cell \mathbf{K}_P^{ce} can be approximated as follows

$$\mathbf{K}_P^{\text{ce}} \approx \beta \cdot \sum_{\text{vo}}^{n_{\text{vo}}} \sum_{\text{sd}}^{n_{\text{vo}, \text{sd}}} \sum_i^{n_{\text{gauss}}^s} \delta_{\text{ce cell}(\mathbf{x}(\xi_i))} \delta_{\text{vo voronoi}(\mathbf{x}(\xi_i))} (\mathbf{N}^T \mathbf{N}) \|\mathbf{J}^{\text{sd}}\|_{\xi_i} v_i. \quad (7)$$

Here n_{gauss}^s denotes the number of Gauss-Legendre points in one dimension while ξ_i and v_i denote the Gauss-Legendre coordinates and weights. The Kronecker delta function δ_{ij} is used to check whether an integration point is contained within the current Voronoi region vo and current mesh cell ce. These checks ensure that the numerical integration approximates the original integral in a consistent manner.

2.4 Challenges, limitations and further remarks

Both, the diffuse and the sharp interface approach presented in the previous section build on the fact that the Voronoi regions exhibit regularities for the point clouds in question. In 2D for smooth boundaries captured with high and approximately equal sampling density we can roughly group the Voronoi regions in two groups as visible in fig. 7 (a). Firstly there are regions which mainly extend into normal direction while being confined in tangential direction [28]. Secondly for $k > 1$ 'bands' of small Voronoi regions form in the vicinity of the medial axis due to fluctuations of $N^k(P, \mathbf{x})$. In regions of the first type the edges of the Voronoi regions should limit the validity of the local approximation plane Γ_{PCA, N^k} . Regions of the second type should arguably neither be included in $\Gamma_{D, \text{PCA}}$ nor $\Gamma_{D, \text{sharp}}$ in. In both approaches r is the control parameter which can be adjusted to reach these two goals.

For point clouds sampled from non-smooth boundaries and/or with varying sampling density distinguishing between these two groups of Voronoi regions is no longer possible. Additionally unfavorable local approximation planes Γ_{PCA, N^k} may exist which leading to discontinuities in $\Gamma_{D, \text{PCA}}$ respectively $\Gamma_{D, \text{sharp}}$. This more general setting is indicated in fig. 7 (b). This is not to forget that

the presence of noise and outliers could worsen situation significantly and lead to very unfavorable boundary approximations.

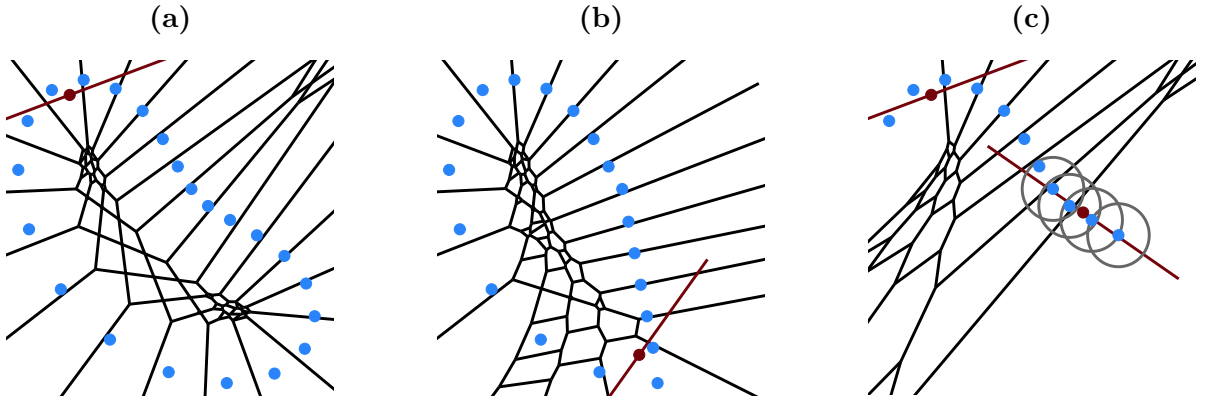


Figure 7: Voronoi diagrams for three different point clouds. Some local approximation planes Γ_{PCA,N^k} in selected Voronoi regions are plotted in red. Circles with favorable radius r displayed in gray.

For point clouds sampled from open boundaries approximation planes at the ends could extend well beyond their intended local reach in the diffuse approach since the no bound l_{max}^s exists. Here it is important to understand that r defines a domain for a point cloud given as the union of disks of radius r around the individual points p_i . For small r this domain truncates Γ_{PCA,N^k} in unfavorably bounded Voronoi regions as indicated in fig. 7 (c). But r also has to be large enough such that this truncation does not introduce unintentional discontinuities in $\Gamma_{D,PCA}$. In a sense the influence of r in our setting can be compared to the influence of α in α -shapes.

α -shapes are related to the union of disks, too, and have been heavily investigated by the computer graphics community as means to reconstruct a surface from a point cloud. There it became apparent that locally refining r is necessary in many cases [29]. Of course other approaches to the problem are possible such as introducing dummy points to bound Voronoi regions [30]. We conclude that it the problem can only reliably be solved with complementary local parameters, especially in the presence of noise. However, local parameters would add many degrees of freedom to the overall approximation $\Gamma_{D,PCA}$. To not complicate the analysis further we opted against introducing more parameters. Moreover we assert that the central deficiency of both approaches in their current version is that they cannot in general be applied to point clouds sampled from open or non-smooth boundaries and restrict the numerical studies accordingly. However, a more detailed study is beyond the scope of this paper. Instead we would like to point out that 2D point cloud curve reconstruction is indeed an active field of research and direct the interested reader to the very recent state of the art review published in [31].

To conclude this section we will briefly discuss the situation in three dimensions. In three dimensions, Voronoi regions are convex, possibly unbounded polyhedrons. Efficient explicit computations with the set of points, edges and polygons that make up these 3D Voronoi diagrams would necessitate further considerations in algorithms and data structures. Additionally, the computation of Voronoi diagrams is challenging as the diagrams have worst case exponential complexity [26].

However, the presented sharp interface approach does not need the explicit computation of Voronoi diagrams. Instead, the presented approach relies on an implicit representation of the zero-level set of $d_{PCA}(P_D, \mathbf{x})$ or $\Gamma_{D,PCA}$. These would be found by octrees. Quadrees can then be used to perform the integrations over the boundary planes Γ_{PCA,N^k} . We would further like to remark that the implicitly reconstructed boundary planes do not even have to possess a C^0 continuity because models with flawed boundaries may also be handled by the FCM [2]. Although these are all promising hints

that an extension to three dimensions might be straight forward, experience shows that only an implementation for 3D will disclose possible pitfalls.

3 Numerical examples

In this section we will investigate two types of examples. Section 3.1 closely investigates a benchmark example known in the community of computational mechanics at which the diffuse interface approach rehearsed in section 2.2 is compared to the newly developed sharp interface approach presented in section 2.3. All algorithms are implemented in the FCMLab framework which documented in [32] and publicly accessible at https://gitlab.lrz.de/cie_sam_public/fcmlab/

In section 3.2 we then apply the sharp interface approach on two point cloud examples taken from a benchmark-series of point clouds [31] which was built for the evaluation of reconstruction algorithms to demonstrate that the algorithm is capable of capturing also examples with convex, concave and non-smoothly boundaries involving kinks.

3.1 Annular plate benchmarks

3.1.1 Problem definition

An annular plate under plane stress conditions with prescribed displacement along the whole boundary is subjected to a body force in radial direction. A detailed illustration of the problem, mesh and analytical solution as given in [33] is depicted in fig. 8. A plot of the solution u_r along the cut line is given in fig. 9.

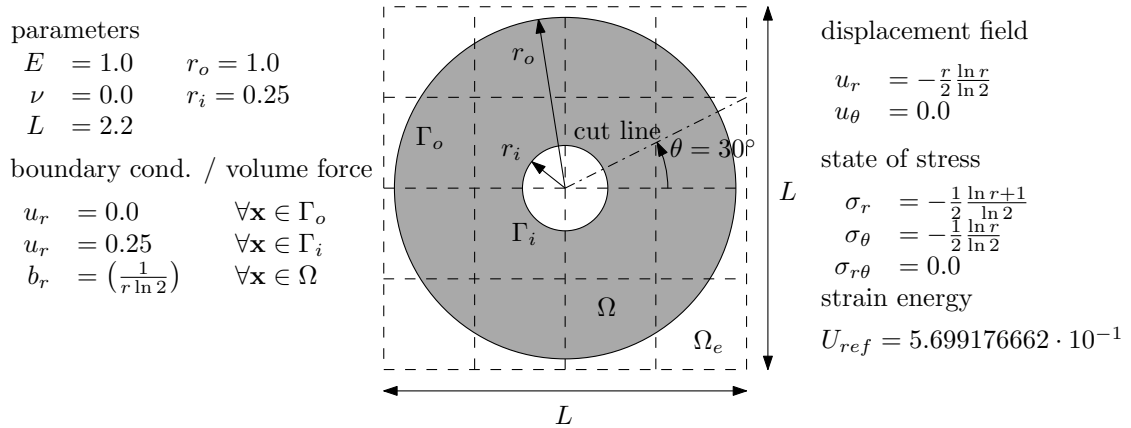


Figure 8: Annular plate setup

Irrespective of the way the penalty integrals in eq. (1) are evaluated the method's effectiveness crucially depends on the choice of β . From other works [34] it is also clear that the diffuse interface approach is very sensitive to the choice of ϵ . Hence a numerical study is now considered that allows to characterize the influence of β on the resulting error while considering ϵ in the diffuse interface approach. The employed error measure is the relative error in the energy norm defined as

$$e = \sqrt{\frac{|U_{num} - U_{ref}|}{U_{ref}}} \cdot 100 [\%]. \quad (8)$$

The mass matrix and load vector for basis functions of polynomial degree 10 were precomputed employing a quadtree of depth 10 and a Gaussian quadrature of 11 points. In this case the indicator function $\alpha(\mathbf{x})$, with $\alpha_{fic} = 10^{-8}$, is constructed from exact circle formulas to minimize the integration

error. These precomputations allow to apply the penalty integrals using the two approaches to the same discrete matrix-vector pair which further enhances their comparability.³

The two point clouds discretizing the boundary with approximately equal sampling density are constructed by taking $n_{points} = 10^4$ points on the inner circle and $4n_{points}$ points on the outer circle. We chose to fix $k = 4$ at all times for the computation of the local approximation planes. For the diffuse interface approach we restrict ϵ to the values $\epsilon_1 = 5 \cdot 10^{-3}$, $\epsilon_2 = 5 \cdot 10^{-4}$ and $\epsilon_3 = 5 \cdot 10^{-5}$. Further, we set $n_{gauss}^\epsilon = 10$ and $n_{sub}^\epsilon = 7$ for ϵ_1 , respectively $n_{sub}^\epsilon = 10$ and $n_{sub}^\epsilon = 13$ for ϵ_2 and ϵ_3 . While for the diffuse interface approach the integration parameters have to be chosen with respect to ϵ the sampling density is decisive for the sharp interface approach. Thus we chose $n_{query}^s = 12$, $n_{sub}^s = 3$, $n_{gauss}^s = 11$ and $l_{max}^s = 3 \cdot 10^{-4}$ in accordance with the problem's sampling density.

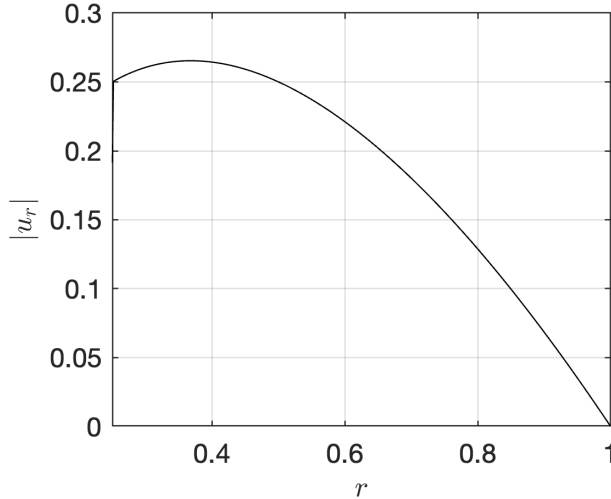


Figure 9: Solution along the radius.

To compute a numerical reference the inner circle is discretized with 10^4 line segments and the outer circle with $4 \cdot 10^4$ line segments respectively. The penalty integrals in eq. (1) are then evaluated by computing a Gaussian quadrature with 11 points on each line segment.

3.1.2 Numerical Results

Building on this setup a β -study is conducted for 26 possible values of β logarithmically spaced between 10 and $5 \cdot 10^6$. The resulting error e for the diffuse interface approach, the sharp interface approach and the numerical reference is plotted in fig. 10.

Contrary to the expectation the error e does not monotonically decrease for the diffuse interface approach when larger values β are employed. While the error corresponds to the error of the numerical reference for small β the error curves level off at certain points and the error increases again. Thus the error will only become minimal for certain optimal values of β . These optimal values depend on the width of the diffuse boundary ϵ . By contrast, the numerical solution for the sharp interface approach converges towards the exact solution at the same rate as the reference solution. The best result of $e \approx 0.04$ is obtained for the sharp interface approach with $\beta = 1.39 \cdot 10^6$, an accuracy which cannot be reached by the diffuse interface approach.

The reason for the convergence behavior of the diffuse interface approach is examined further next. The point clouds discretizing the inner and outer circle were chosen with a very high sampling density. Therefore a geometric mismatch between Γ_D and $\Gamma_{D,PCA}$ can be ruled out as primary cause

³In line with a reviewer remark we would like to comment that it is of course possible to choose any other type of discretization also combined with local refinements as, e.g. presented in [35, 36, 37] but opted not to do so out of simplicity.

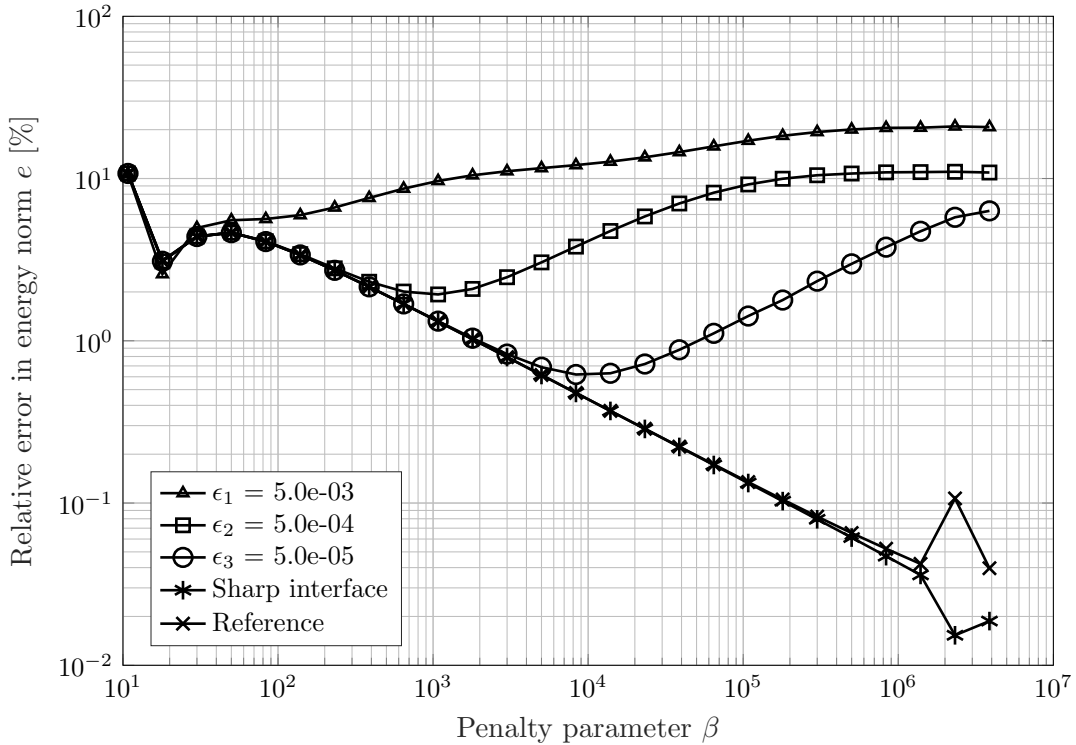


Figure 10: β -study

of the error. This is also supported by the results for the sharp interface approach since it integrates over $\Gamma_{D,sharp} \approx \Gamma_{D,PCA}$.

But no matter how the penalty integrals are computed β controls the extent to which deviations from the constraint are penalized. Therefore, the attainable error below the tear off point is limited by β itself. For large β the constraint is enforced to some extent on the diffuse layer Γ_D^ϵ , too. In other words, controlling the Dirichlet boundary condition is also constraining the Neumann boundary condition. This undesirable constraining of the gradient towards zero in normal direction as exemplarily depicted in fig. 12. This unintended side effect is stronger for larger ϵ and larger β . Due to this situation a local minimum of the error e in between small and large β exists if ϵ is small enough. This situation is depicted for ϵ_3 in fig. 11. The finding that in a diffuse boundary approach only one problem dependent choice of β exists for small enough ϵ is consistent with results by other researchers [34] [38].

Very small values of ϵ are necessary to minimize constraining the gradient. This, in turn, requires costlier numerical integration with a higher subdivision level n_{sub}^ϵ . A trade-off between integration effort and accuracy results in the fact that the diffuse interface approach is not only less accurate but also computationally more expensive compared to the sharp interface method. Moreover, the range of β values leading to favorable results is not known beforehand given a specific problem and a value of ϵ .

The side effect of constraining the gradient does not exist for the sharp interface approach by construction. Larger values for β consistently yield lower errors. Figure 13 exemplarily depicts the error in u_x . While both approaches start with the same ad hoc boundary approximation $d_{PCA}(P, \mathbf{x})$ they diverge in the way integration points are distributed in the vicinity of $\Gamma_{D,PCA}$. In this example Gauss quadrature is applied to 2D sub-cells of quadtrees for the diffuse interface approach. In the sharp interface approach Gauss quadrature is applied to line segments resulting in much less integration points. Hence the sharp interface approach does not only evade the trade off between

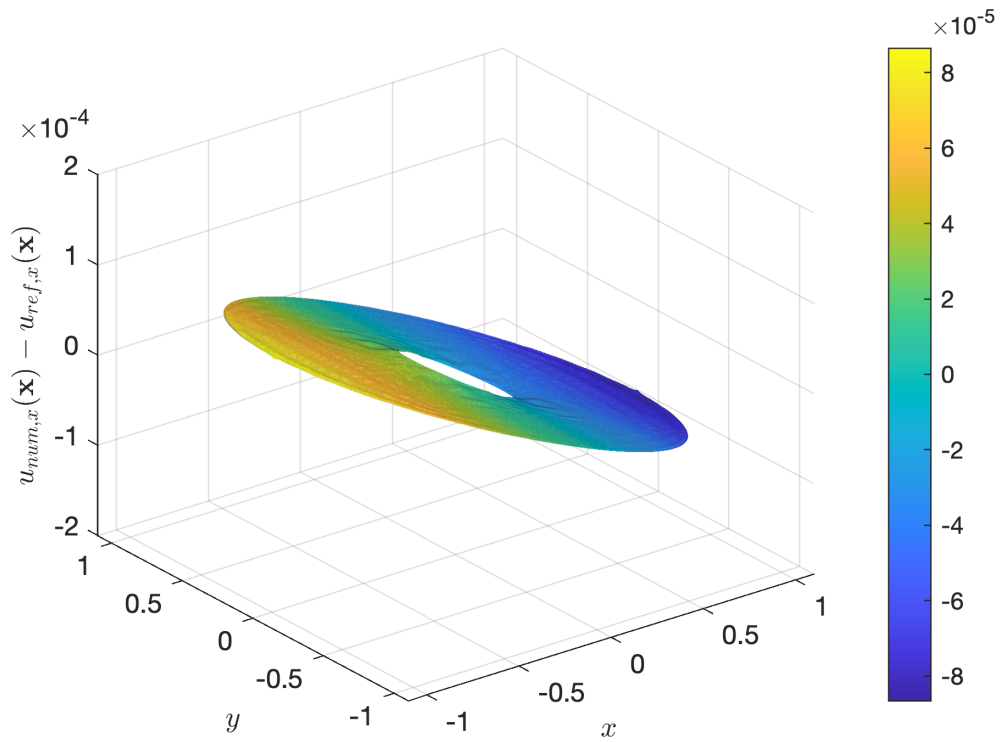


Figure 11: Abs. error in u_x for the diffuse interface approach with ϵ_3 and $\beta = 8043$

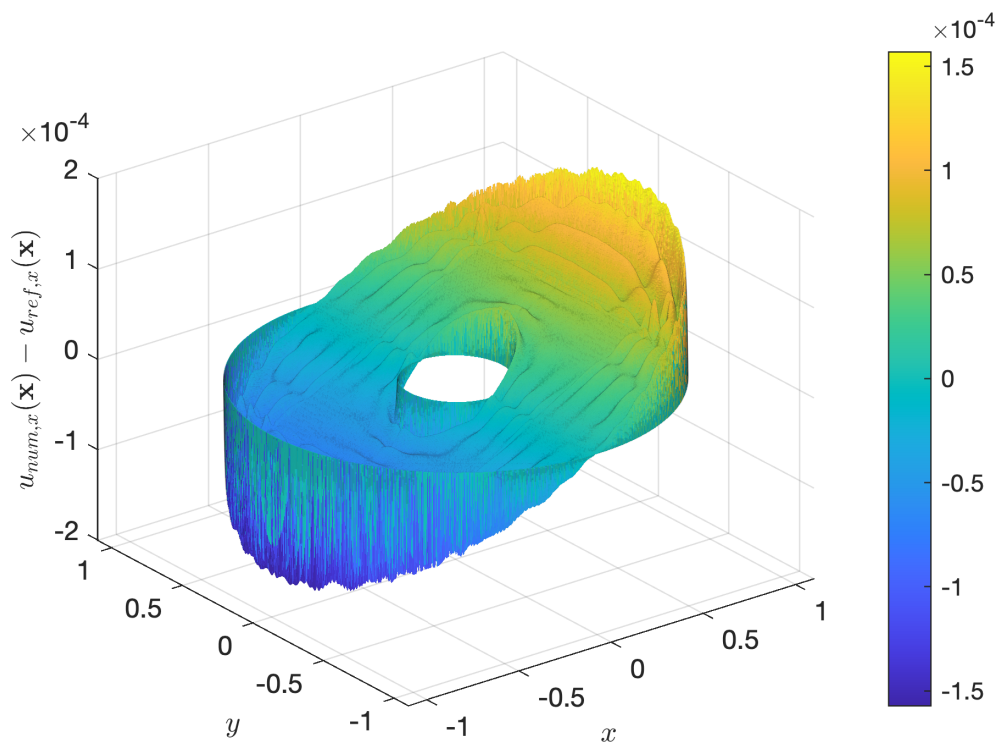


Figure 12: Abs. error in u_x for the diffuse interface approach with ϵ_3 and $\beta = 5 \cdot 10^5$

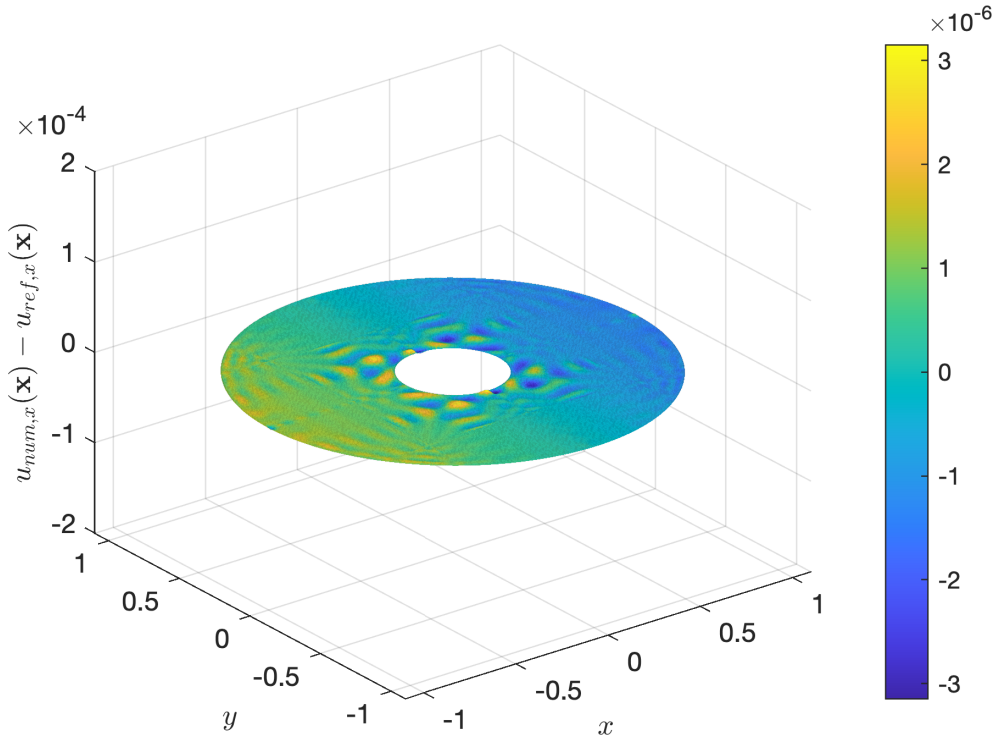


Figure 13: Abs. error in u_x for the sharp interface approach with $\beta = 5 \cdot 10^5$

integration effort and accuracy but implies a lower computational effort by construction.

3.2 Point clouds resembling concave, convex and non-smooth boundaries

To study the practicability of the sharp interface approach we investigate a membrane structure with prescribed deflection on the approximated boundary $\Gamma_{D,sharp}$. The problem can be modeled with Poisson's equation. Incorporating the prescribed deflection via the penalty method leads to the following weak formulation "Find $u \in H^1(\Omega)$ such that

$$(\nabla u, \nabla w)_\Omega + \beta \cdot (u, w)_{\Gamma_{D,sharp}} = -\left(\frac{p}{\sigma_0 t}, w\right)_\Omega + \beta \cdot (u, \hat{u})_{\Gamma_{D,sharp}} \quad \forall w \in H^1(\Omega)." \quad (9)$$

Here u, w and \hat{u} denote the deflection, the test function and the prescribed deflection, respectively. The vertical load, prestress and thickness are given by p, σ_0 and t .

The point clouds in question are taken from the benchmark by Ohrhallinger et al. [31] and may be found at <https://gitlab.com/stefango74/curve-benchmark>. The point clouds are scaled such that they fit into the solution domain $[-1.1, 1.1] \times [-1.1, 1.1]$ which is discretized by 16×16 elements of polynomial degree 10. The solution is fixed to zero along the mesh boundary. Further we chose $\beta = 1 \cdot 10^6$, $\frac{p}{\sigma_0 t} = 10$, $\hat{u} = 1$, $k = 4$ and employ a Gaussian quadrature of 11 points throughout all parts of the example.

The first example `mc4.txt` consists of multiple convex and concave curves and is depicted in fig. 14a. Since all curves are smooth, closed and sampled with approximately equal sampling density the point cloud is favorable with regard to section 2.4. Nevertheless the example poses a challenge due to the structure of the Voronoi diagram. The Voronoi regions whose approximation planes Γ_{PCA, N^k} we want to include extend in normal direction while being confined in tangential direction as visible in fig. 14a. Due to fluctuations of $N^k(P, \mathbf{x})$ 'bands' of small Voronoi regions form in the vicinity of the medial axis which we do not want to include in $\Gamma_{D,sharp}$.

Thus the challenge is to select the radius r just right to include all Voronoi regions in the former

group while excluding those in the latter. We find that this division is in fact possible for $r = 0.02$ and a query quadtree of depth $n_{query}^s = 5$ per mesh cell. The approximation planes Γ_{PCA, N^k} initialized with $l_{max}^s = 8 \cdot 10^{-2}$ and bisected to level $n_{sub}^s = 4$ are plotted in fig. 14a. The approximated boundary is continuous and smooth except in places with high curvature. Figure 14b shows that this overall choice of parameters is sufficient to apply the constraint along the point cloud.

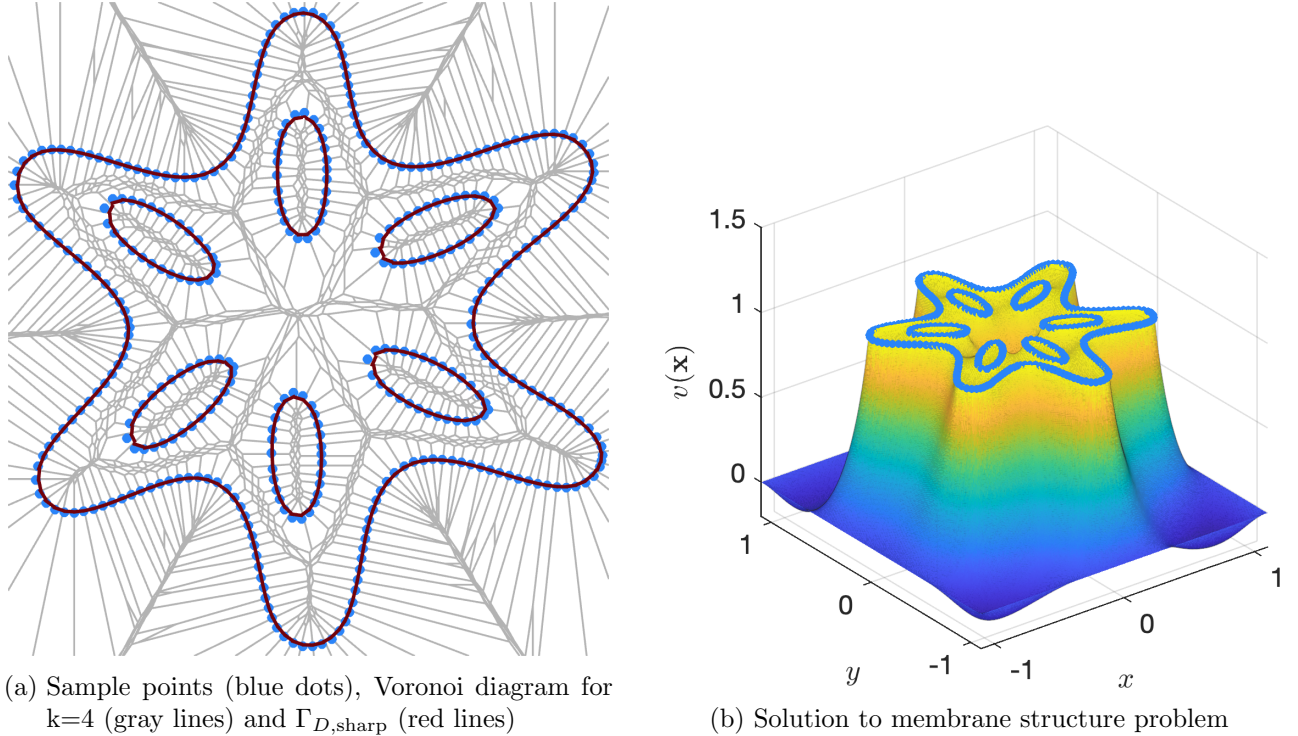


Figure 14: Example `mc4.txt`

The second example `oc16.txt` is shown in fig. 15a. It consists of one 'snakelike' open curve with many non-smooth kinks sampled with slightly varying sampling density. Considering section 2.4 the characteristics of the approximated boundary on the kinks and open ends are of interest here.

The approximated boundary for $r = 0.035$, $n_{query}^s = 5$, $l_{max}^s = 8 \cdot 10^{-2}$ and $n_{sub}^s = 4$ is shown in fig. 15b. Separating the two groups of Voronoi regions that likewise exist in this case is not possible. We opt to choose r relatively tight to filter all non wanted Voronoi regions in the vicinity of the medial axis. Subsequently we miss one Voronoi region that should be included (green square in fig. 15b). While the open ends and kinks are handled satisfactory the approximated boundary shows several small discontinuities.

Clearly the sharp interface approach does not in general yield watertight, continuous reconstructions as one might wish for in a e.g. in a computer graphics context. But this was also not our original intent. Our goal was to apply Dirichlet boundary conditions on domains defined by point clouds in the context of partial differential equations. The implied smoothness of possible solutions to such equation systems in combination with the weak nature of the penalty method allow for reduced requirements for the approximated boundary.

Remark: Remember that the Voronoi diagram is actually never constructed. It is only approximated implicitly from $N^k(P, \mathbf{x})$ as described by fig. 5 and fig. 6. Nevertheless, we plot its outline in gray because this gives a good impression on how the red sharp boundary boundary is reconstructed.

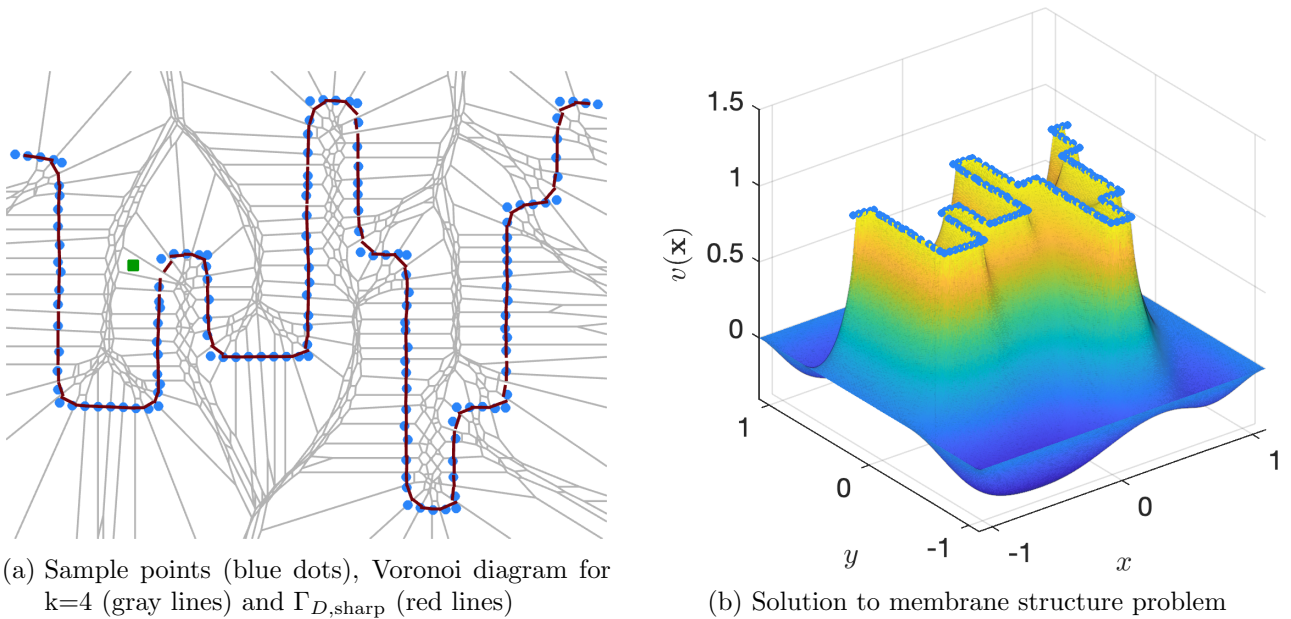


Figure 15: Example oc16.txt

4 Conclusions

Solving contour integrals on non-boundary-conforming meshes is essential to apply boundary conditions in embedded domain methods such as the finite cell method. In [10] an approach is presented where the domain is solely defined by a set of points. Therein, Neumann boundary conditions are applied by implicitly approximating non-zero Neumann boundaries using the diffuse interface approach.

This contribution builds upon this idea but modifies it in such a way that the same local approximation can be integrated without assuming a diffuse interface. In essence this can be achieved by closely examining the implicit boundary approximation and interpreting it with respect to order- k Voronoi diagrams. Both approaches are compared in a numerical example for the case of enforcing Dirichlet boundary conditions with the penalty method. Therein it becomes apparent that the diffuse interface approach inherently suffers from a trade-off between integration effort and accuracy which is completely eliminated in the newly presented sharp interface approach. Therefore, the sharp interface approach should be preferred wherever possible.

Acknowledgements

The last author gratefully acknowledges the financial support of the German Research Foundation (DFG) under grant KO 4570/1-1.

References

- [1] M. Mäntylä, *An introduction to solid modeling*. No. 13 in Principles of computer science series, Rockville: Computer Science Press, 1988.
- [2] B. Wassermann, S. Kollmannsberger, S. Yin, L. Kudela, and E. Rank, “Integrating CAD and numerical analysis: ‘Dirty geometry’ handling using the Finite Cell Method,” *Computer Methods in Applied Mechanics and Engineering*, vol. 351, pp. 808–835, July 2019.
- [3] F. Massarwi and G. Elber, “A B-spline based framework for volumetric object modeling,” *Computer-Aided Design*, vol. 78, pp. 36–47, Sept. 2016.
- [4] Y. J. Zhang, *Geometric Modeling and Mesh Generation From Scanned Images*. Chapman & Hall/CRC mathematical and computational imaging sciences, Chapman & Hall/CRC, 2016.
- [5] T. de Geus, J. Vondřejc, J. Zeman, R. Peerlings, and M. Geers, “Finite strain FFT-based non-linear solvers made simple,” *Computer Methods in Applied Mechanics and Engineering*, vol. 318, pp. 412–430, May 2017.
- [6] N. Korshunova, J. Jomo, G. Lékó, D. Reznik, P. Balázs, and S. Kollmannsberger, “Image-based material characterization of complex microarchitected additively manufactured structures,” *Computers & Mathematics with Applications*, vol. 80, pp. 2462–2480, Dec. 2020.
- [7] N. Korshunova, G. Alaimo, S. Hosseini, M. Carraturo, A. Reali, J. Niiranen, F. Auricchio, E. Rank, and S. Kollmannsberger, “Bending behavior of octet-truss lattice structures: Modelling options, numerical characterization and experimental validation,” *Materials & Design*, vol. 205, p. 109693, July 2021.
- [8] H. Gravenkamp, A. A. Saputra, and S. Eisenträger, “Three-dimensional image-based modeling by combining SBFEM and transfinite element shape functions,” *Computational Mechanics*, vol. 66, pp. 911–930, Oct. 2020.
- [9] J. A. Cottrell, T. J. R. Hughes, and Y. Bazilevs, *Isogeometric Analysis: Toward Integration of CAD and FEA*. John Wiley & Sons, Aug. 2009.
- [10] L. Kudela, S. Kollmannsberger, U. Almac, and E. Rank, “Direct structural analysis of domains defined by point clouds,” *Computer Methods in Applied Mechanics and Engineering*, vol. 358, p. 112581, Jan. 2020.
- [11] V. Saul’ev, “Saul’ev, V.K.: On solution of some boundary value problems on high performance computers by fictitious domain method. Sibirian Math. J. 4, 912–925 (1963),” *Sibirian Mathematical Journal*, vol. 4, pp. 912–925, 1963.
- [12] E. Burman, S. Claus, P. Hansbo, M. G. Larson, and A. Massing, “CutFEM: Discretizing geometry and partial differential equations,” *International Journal for Numerical Methods in Engineering*, vol. 104, pp. 472–501, Nov. 2015.
- [13] M. Breitenberger, A. Apostolatos, B. Philipp, R. Wüchner, and K. U. Bletzinger, “Analysis in computer aided design: Nonlinear isogeometric B-Rep analysis of shell structures,” *Computer Methods in Applied Mechanics and Engineering*, vol. 284, pp. 401–457, Feb. 2015.

- [14] D. Kamensky, M.-C. Hsu, D. Schillinger, J. A. Evans, A. Aggarwal, Y. Bazilevs, M. S. Sacks, and T. J. R. Hughes, “An immersogeometric variational framework for fluid–structure interaction: Application to bioprosthetic heart valves,” *Computer Methods in Applied Mechanics and Engineering*, vol. 284, pp. 1005–1053, Feb. 2015.
- [15] S. Badia, F. Verdugo, and A. F. Martín, “The aggregated unfitted finite element method for elliptic problems,” *Computer Methods in Applied Mechanics and Engineering*, vol. 336, pp. 533–553, 2018.
- [16] A. Düster, J. Parvizian, Z. Yang, and E. Rank, “The finite cell method for three-dimensional problems of solid mechanics,” *Computer Methods in Applied Mechanics and Engineering*, vol. 197, pp. 3768–3782, Aug. 2008.
- [17] A. Düster, E. Rank, and B. A. Szabó, “The p-version of the finite element method and finite cell methods,” in *Encyclopedia of Computational mechanics* (E. Stein, R. Borst, and T. J. R. Hughes, eds.), vol. 2, pp. 1–35, Chichester, West Sussex: John Wiley & Sons, 2017.
- [18] A. Longva, F. Lössner, T. Kugelstadt, J. A. Fernández-Fernández, and J. Bender, “Higher-order finite elements for embedded simulation,” *ACM Transactions on Graphics*, vol. 39, pp. 181:1–181:14, Nov. 2020.
- [19] I. Babuska, “The Finite Element Method with Penalty,”
- [20] D. Schillinger, I. Harari, M.-C. Hsu, D. Kamensky, S. K. F. Stoter, Y. Yu, and Y. Zhao, “The non-symmetric Nitsche method for the parameter-free imposition of weak boundary and coupling conditions in immersed finite elements,” *Computer Methods in Applied Mechanics and Engineering*, vol. 309, pp. 625–652, Sept. 2016.
- [21] S. Kollmannsberger, A. Özcan, J. Baiges, M. Ruess, E. Rank, and A. Reali, “Parameter-free, weak imposition of Dirichlet boundary conditions and coupling of trimmed and non-conforming patches,” *International Journal for Numerical Methods in Engineering*, vol. 101, pp. 670–699, Mar. 2015.
- [22] N. Amenta, M. Bern, and M. Kamvysselis, “A new Voronoi-based surface reconstruction algorithm,” in *Proceedings of the 25th Annual Conference on Computer Graphics and Interactive Techniques - SIGGRAPH '98*, (Not Known), pp. 415–421, ACM Press, 1998.
- [23] X. Li, J. Lowengrub, A. R. Tz, and A. Voigt, “SOLVING PDES IN COMPLEX GEOMETRIES: A DIFFUSE DOMAIN APPROACH,” p. 27.
- [24] A. Rätz and A. Voigt, “PDE’s on surfaces—a diffuse interface approach,” *Communications in Mathematical Sciences*, vol. 4, no. 3, pp. 575–590, 2006.
- [25] H. G. Lee and J. Kim, “Regularized Dirac delta functions for phase field models,” *International Journal for Numerical Methods in Engineering*, vol. 91, pp. 269–288, July 2012.
- [26] F. Aurenhammer, R. Klein, and D.-T. Lee, *Voronoi Diagrams and Delaunay Triangulations*. 2013.
- [27] D. Schmitt and J.-C. Spehner, “Order-k Voronoi Diagrams, k-Sections, and k-Sets,” in *Discrete and Computational Geometry* (G. Goos, J. Hartmanis, J. van Leeuwen, J. Akiyama, M. Kano, and M. Urabe, eds.), vol. 1763, pp. 290–304, Berlin, Heidelberg: Springer Berlin Heidelberg, 2000.

- [28] T. K. Dey and L. Wang, “Voronoi-based feature curves extraction for sampled singular surfaces,” *Computers & Graphics*, vol. 37, pp. 659–668, Oct. 2013.
- [29] H. Edelsbrunner, D. Kirkpatrick, and R. Seidel, “On the shape of a set of points in the plane,” *IEEE Transactions on Information Theory*, vol. 29, pp. 551–559, July 1983.
- [30] P. Alliez, D. Cohen-Steiner, Y. Tong, and M. Desbrun, “Voronoi-based Variational Reconstruction of Unoriented Point Sets,” p. 10.
- [31] S. Ohrhallinger, J. Peethambaran, A. D. Parakkat, T. K. Dey, and R. Muthuganapathy, “2D Points Curve Reconstruction Survey and Benchmark,” *Computer Graphics Forum*, vol. 40, pp. 611–632, May 2021.
- [32] N. Zander, T. Bog, M. Elhaddad, R. Espinoza, H. Hu, A. Joly, C. Wu, P. Zerbe, A. Düster, S. Kollmannsberger, J. Parvizian, M. Ruess, D. Schillinger, and E. Rank, “FCMLab: A finite cell research toolbox for MATLAB,” *Advances in Engineering Software*, vol. 74, pp. 49–63, Aug. 2014.
- [33] N. Zander, S. Kollmannsberger, M. Ruess, Z. Yosibash, and E. Rank, “The Finite Cell Method for linear thermoelasticity,” *Computers & Mathematics with Applications*, vol. 64, pp. 3527–3541, Dec. 2012.
- [34] L. H. Nguyen, S. K. Stoter, M. Ruess, M. A. Sanchez Uribe, and D. Schillinger, “The diffuse Nitsche method: Dirichlet constraints on phase-field boundaries,” *International Journal for Numerical Methods in Engineering*, vol. 113, pp. 601–633, Jan. 2018.
- [35] N. Zander, T. Bog, S. Kollmannsberger, D. Schillinger, and E. Rank, “Multi-level hp-adaptivity: high-order mesh adaptivity without the difficulties of constraining hanging nodes,” *Computational Mechanics*, vol. 55, pp. 499–517, Feb. 2015.
- [36] D. D’Angella, S. Kollmannsberger, E. Rank, and A. Reali, “Multi-level Bézier extraction for hierarchical local refinement of Isogeometric Analysis,” *Computer Methods in Applied Mechanics and Engineering*, vol. 328, pp. 147–174, Jan. 2018.
- [37] P. Kopp, E. Rank, V. M. Calo, and S. Kollmannsberger, “Efficient multi-level hp-finite elements in arbitrary dimensions,” *arXiv:2106.08214 [cs, math]*, June 2021.
- [38] M. Burger, O. L. Elvetun, and M. Schlottbom, “Analysis of the Diffuse Domain Method for Second Order Elliptic Boundary Value Problems,” *Foundations of Computational Mathematics*, vol. 17, pp. 627–674, June 2017.